Effect of surface waviness and aspect ratio on heat transfer inside a wavy enclosure

Prodip Kumar Das
Department of Mechanical Engineering, University of Alberta, Edmonton, Alberta, Canada

Shohel Mahmud and Syeda Humaira Tasnim
Department of Mechanical Engineering, University of Waterloo, Waterloo, Ontario, Canada

A.K.M. Sadrul Islam
Department of Mechanical Engineering, Bangladesh University of Engineering and Technology (BUET), Dhaka, Bangladesh

Received January 2003
Revised May 2003
Accepted June 2003

Keywords *Convection, Finite volume methods, Heat transfer, Surface texture*

Abstract *A numerical simulation has been carried out to investigate the buoyancy induced flow and heat transfer characteristics inside a wavy walled enclosure. The enclosure consists of two parallel wavy and two straight walls. The top and the bottom walls are wavy and kept isothermal. Two straight-vertical sidewalls are considered adiabatic. Governing equations are discretized using the control volume based finite-volume method with collocated variable arrangement. Simulation was carried out for a range of surface waviness ratios,* λ = 0.00-0.25; *aspect ratios, A = 0.25-0.5; and Rayleigh numbers Ra =* 10^0-10^7 *for a fluid having Prandtl number equal to 1.0. Results are presented in the form of local and global Nusselt number distributions, streamlines, and isothermal lines for different values of surface waviness and aspect ratios. For a special case of* $\lambda = 0$ *and A= 1.0, the average Nusselt number distribution is compared with available reference. The results suggest that natural convection heat transfer is changed considerably when surface waviness changes and also depends on the aspect ratio of the domain. In addition to the heat transfer results, the heat transfer irreversibility in terms of Bejan number (Be) was measured. For a set of selected values of the parameters (*λ*, A, and Ra), a contour of the Bejan number is presented at the end of this paper.*

Nomenclature

A = aspect ratio (= δ/L)
Be = Bejan number (see equation (24))
Br = Brinkman number (= Ec × Pr)
$\mathbf{g}$ = gravity vector, m s^{-2}
Ec = Eckert number
Gr = Grashof number, (= $\rho^2 g\beta\Delta T\delta^3/\mu^2$)
h = heat transfer coefficient, W m^{-2}K^{-1}
k = thermal conductivity, W m^{-1}K^{-1}
L = horizontal length of the wave, m
Nu = Nusselt number
$\hat{\mathbf{n}}$ = unit normal vector
Pr = Prandtl number (= ν/κ)

We would like to thank Patrick Kirchen and Shahnawaz Hossain Molla (Department of Mechanical Engineering, University of Alberta, Canada) for different kinds of support they gave during this research.

International Journal of Numerical Methods for Heat & Fluid Flow
Vol. 13 No. 8, 2003
pp. 1097-1122

0961-5539
DOI 10.1108/09615530310501975

P = dimensionless pressure
Ra = Rayleigh number, ($= Gr \times Pr$)
T = temperature, K
U = dimensionless velocity component in the x-direction
V = dimensionless velocity component in the y-direction
x = horizontal coordinate
X = dimensionless horizontal coordinate
y = vertical coordinate
Y = dimensionless vertical coordinate

Greek symbols

α = amplitude of the top and the bottom walls, m
β = thermal expansion coefficient, K^{-1}
δ = inter wall spacing between the top and bottom walls, m
λ = surface waviness ratio, ($= \alpha/L$)
κ = thermal diffusivity, $m^2 s^{-1}$
ν = kinematic viscosity, $m^2 s^{-1}$
ρ = density of the fluid, $kg\,m^{-3}$
Φ = irreversibility distribution ratio
Ω = dimensionless temperature difference
Θ = dimensionless temperature

Subscript

av = average value
∞ = at ambient condition
C = average value based on cold wall
H = average value based on hot wall
L = local value
W = value at the wall
0 = reference value
Δ = difference between the two values

Introduction

Free or forced convection heat transfer inside geometries of regular shape (rectangular channel, circular pipe, etc.) has many significant engineering applications, for example, double-wall thermal insulation, underground cable systems, solar-collectors, electric machinery, cooling systems of micro-electronic devices, natural circulation in the atmosphere, the molten core of the earth, etc. A considerable number of published articles are available that deal with flow characteristics, heat transfer, flow and heat transfer instability, transition to turbulence, design aspects, etc. Curious readers are suggested to read the paper by Yang (1987) for a comprehensive reference. On the other hand, studies dealing with convection problems inside more complex geometries have been rather limited. The phrase *complex geometry* covers different types of geometric configurations, namely L-shaped cavities (Mahmud, 2002), trapezoidal cavities (Peric, 1993), arc shaped enclosures (Chen and Cheng, 2002), wavy cavities (Mahmud *et al.*, 2002c), triangular cavities (Poulikakos and Bejan, 1983), etc. Flow and heat transfer analyses inside such geometry is a comparatively difficult task either experimentally or analytically (or numerically). Therefore, less effort has been given to analyze flow and thermal characteristics inside complex shaped geometry for the past several decades. The primary focus is to analyze the flow and thermal characteristics inside a special class of complex shaped geometry, i.e. a geometry with wavy walls that follows a well-defined mathematical function (sine or cosine). Enclosures with wavy walls have always been less attractive to researchers due to their complex fluid dynamic behavior as well as their geometrical complexity. Sobey (1980a) published numerical results with an experimental verification (Sobey, 1980b) of flow patterns inside a furrowed channel. A furrowed channel is a special type of channel with wavy wall that

follows the cosine function. Later, Sobey extended his work by calculating oscillatory flow pattern inside the same geometry (Sobey, 1982). Further extension is done by Sobey (1983) by calculating the flow separation characteristics inside the wavy walled channel. The fluid dynamics of the separation phenomenon inside the wavy walled channels is still incomplete, thus motivating some researchers to extend the work of Sobey (1983), for example, Leneweit and Auerbach (1999) and Mahmud *et al.* (2002a,b). The foregoing discussions that have dealt with problems of wavy walled channels are very much restricted to fluid flow only. A limited number of forced convection heat transfer results are reported by Russ and Beer (1997a,b) and Wang and Vanka (1995) whereas considerable attention has been devoted towards the analyses of laminar steady heat transfer and fluid flow inside complex shaped domains over the past two decades. However, there is limited literature dealing with natural convection inside wavy wall domain. Fabrication of devices with wavy walls depend on the parameters like amplitude, wavelength, phase angle, inter-wall spacing etc. Each of these parameters significantly affects the hydrodynamic and thermal behavior of the fluid inside it.

In our earlier work (Mahmud *et al.*, 2002c), we have shown the effect of surface waviness on natural convection heat transfer and fluid flow inside a vertical wavy walled enclosure for a range of wave ratio ($0.00 \leq \lambda \leq 0.4$) and aspect ratio ($1.0 \leq A \leq 2.0$). We reported a decrease in average heat transfer with the increase of surface waviness. For the horizontal in-phase wavy walled enclosure (Das and Mahmud, 2003), hydrodynamic and thermal behaviors of the fluid inside the enclosure have been investigated for a fixed aspect ratio. In that investigation, we explored the change of true periodic nature of the local Nusselt number distribution with the increase of amplitude-wavelength ratio, but we have not seen any significant influence on the average heat transfer rate due to the surface waviness. One of our interesting findings was the increase of average heat transfer with the increase of surface waviness from zero to a certain value. Recently, Adjlout *et al.* (2002) discussed natural convection in an inclined cavity with hot wavy wall and cold flat wall. They showed the decrease in average heat transfer with the surface waviness when compared with flat wall cavity. However, in their report, they showed result for the grid of 42×42 with an error level of 1.64 percent whereas heat transfer increased by only a small amount when compared to their error level.

Several research works have been conducted for convection heat transfer inside enclosure or channel with wavy walls. Among them, Kumar (2000) presented the parametric results of flow and thermal fields inside a vertical wavy enclosure with porous media. Kumar (2000) concluded that the surface temperature was very sensitive to drifts in the surface undulations, phase of the wavy surface and number of the wave. Hadjadj and Kyal (1999) numerically examined the effect of sinusoidal protuberances on heat

transfer and fluid flow inside an annular space using a non-orthogonal coordinate transformation. In their study, it was reported that both the local and average heat transfer increase with the increase of protuberance amplitude and Rayleigh number, and decreasing Prandtl number. Yao (1983) presented the near wall characteristics of flow and thermal field of a vertical wavy wall. Saidi *et al.* (1987) presented numerical and experimental results of flow over, and heat transfer from, a sinusoidal cavity. They reported that the total heat exchange between the wavy wall of the cavity and the flowing fluid was reduced by the presence of vortex. The vortex plays the role of a thermal screen, which creates a large region of uniform temperature in the bottom of the cavity. Asako and Faghri (1987) and Mahmud *et al.* (2001) gave a finite-volume prediction of heat transfer and fluid flow characteristics inside a wavy walled duct and tube, respectively. Lage and Bejan (1990) documented heat transfer results near a periodically (timewise and spatial) stretching wall. Hossain and Rees (1999), Moulic and Yao (1989) and Rees and Pop (1995) presented similar solutions for natural convection flow near wavy surface at different boundary conditions. Aydin *et al.* (1999), Elsherbiny (1996), Hamady *et al.* (1989), Ozoe *et al.* (1975) and Sundstrom and Kimura (1996) presented results of heat transfer characteristics inside the rectangular enclosures at different aspect ratios and orientations without surface waviness.

In this study, we have presented numerical results based on the finite-volume analysis for laminar natural convection inside a cavity, which consists of two wavy surfaces with different amplitude-wavelength ratios and aspect ratios. Rate of heat transfer in terms of local and global Nusselt numbers are calculated for different Rayleigh numbers. Flow and thermal fields are analyzed by parametric presentation of streamlines and isothermal lines.

Mathematical modeling

In this section, we present the mathematical formulation of the problem considered in terms of the continuity, momentum, and energy equations, and the pertinent boundary conditions for a wavy domain containing two wavy and two flat surfaces. We begin by considering two-dimensional laminar natural convection of an incompressible and Newtonian fluid in a cavity as shown in Figure 1. Distance between the two straight walls is L, two wavy walls is δ, and α is the amplitude of the wavy walls. Modeling the flow as "Boussinesq-incompressible" to take into account the coupling between the energy and momentum equations, we regard the density ρ as constant everywhere except in the buoyancy term of momentum equations (equation (3)). Correspondingly, the non-dimensional equations governing the conservation of mass, momentum and energy in the cavity of Figure 1 are as follows

$$\frac{\partial U}{\partial X} + \frac{\partial V}{\partial Y} = 0. \tag{1}$$

$$\frac{\partial U}{\partial \tau} + U\frac{\partial U}{\partial X} + V\frac{\partial U}{\partial Y} = -\frac{\partial P}{\partial X} + \sqrt{\frac{\mathrm{Pr}}{\mathrm{Ra}}}\left(\frac{\partial^2 U}{\partial X^2} + \frac{\partial^2 U}{\partial Y^2}\right). \tag{2}$$

$$\frac{\partial V}{\partial \tau} + U\frac{\partial V}{\partial X} + V\frac{\partial V}{\partial Y} = -\frac{\partial P}{\partial Y} + \Theta + \sqrt{\frac{\mathrm{Pr}}{\mathrm{Ra}}}\left(\frac{\partial^2 V}{\partial X^2} + \frac{\partial^2 V}{\partial Y^2}\right). \tag{3}$$

$$\frac{\partial \Theta}{\partial \tau} + U\frac{\partial \Theta}{\partial X} + V\frac{\partial \Theta}{\partial Y} = \frac{1}{\sqrt{\mathrm{PrRa}}}\left(\frac{\partial^2 \Theta}{\partial X^2} + \frac{\partial^2 \Theta}{\partial Y^2}\right). \tag{4}$$

Equations (1)-(4) are put into their dimensionless forms by scaling different lengths with average inter wall spacing between the top and the bottom walls (δ), velocity components with reference velocity (V_0) which is equal to $(g\beta\Delta T\delta)^{1/2}$, pressure with ρV_0^2. time with δ/V_0. The dimensionless temperature can be defined as $\Theta = (T - T_\infty)/\Delta T$ where ΔT is equal to $(T_H - T_C)$.

Boundary and initial conditions

Figure 1 shows the computational grid structure and the geometry under consideration in the present investigation along with the coordinate framework and different boundary conditions. The surface shape of the wavy walls follows the profile given in equations (5) and (6). The hot and cold wall temperatures are T_H and T_C, respectively. Initial fluid temperature inside the cavity is taken as T_∞. The initial temperature of the adiabatic walls is set equal to the initial fluid temperature (T_∞) inside the cavity. The gravity acceleration **g** is acted downwards. No slip boundary condition is applied for velocity components at each wall. For the present investigation, boundary conditions are summarized by the following equations:

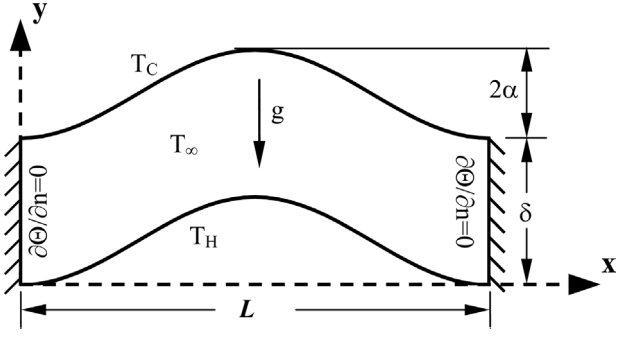

Figure 1.
Schematic representation of the computational geometry under consideration with boundary conditions

$$0 \le X^* \le 1 \quad \text{and}$$
$$0 \le Y^* \le \lambda[1 - \cos(2\pi X^*)] : U = V = 0. \quad \Theta = 1. \tag{5}$$

$$0 \le X^* \le 1 \quad \text{and}$$
$$A \le Y^* \le A + \lambda[1 - \cos(2\pi X^*)] : U = V = 0. \quad \Theta = 0. \tag{6}$$

$$X^* = 0 \quad \text{and} \quad 0 \le Y^* \le A : U = V = 0. \quad \frac{\partial \Theta}{\partial n} = 0. \tag{7}$$

$$X^* = 1 \quad \text{and} \quad 0 \le Y^* \le A : U = V = 0. \quad \frac{\partial \Theta}{\partial n} = 0. \tag{8}$$

where X^* (= XA) and Y^* (= YA) are modified dimensionless horizontal and vertical lengths.

Numerical methodology

To conduct a numerical simulation for the thermofluid dynamics fields, we used the technique similar to that Hortmann *et al.* (1990) based on the finite-volume method as described in Ferziger and Peric (1996). The finite-volume method starts from the conservation equation in integral form as

$$\int_S \rho\phi\, \mathbf{v} \cdot \hat{\mathbf{n}}\, dS = \int_S \Gamma\, \mathrm{grad}\phi \cdot \hat{\mathbf{n}}\, dS + \int_V q_\phi\, dV. \tag{9}$$

where ϕ is any variable, Γ is the diffusivity for the quantity ϕ, and q_ϕ is the source or sink of ϕ.

The solution domain is subdivided into a finite number of contiguous quadrilateral control volumes (CV). The CVs are defined by coordinates of their vertices, which are assumed to be connected by straight lines. This simple form is possible due to the fact that the equations contain no curvature terms and only the projections of the CV faces onto the Cartesian coordinates surfaces are required in the course of discretization, as demonstrated below. All the dependent variables solved for and all fluid properties are stored in the CV center (collocated arrangement). A suitable spatial distribution of dependent variables is assumed and the conservation equations (1)-(4) are applied to each CV, leading to a system of non-linear algebraic equations. The main steps of discretization procedure to calculate convection and diffusion fluxes and source terms are outlined below.

The mass flux through the cell face "e" (Figure 2) is evaluated as

$$\dot{m}_e = \int_{S_e} \rho V\, dS \approx (\rho V)_e \mathbf{S_{1e}} = \rho_e \left(US_1^x + VS_1^y\right). \tag{10}$$

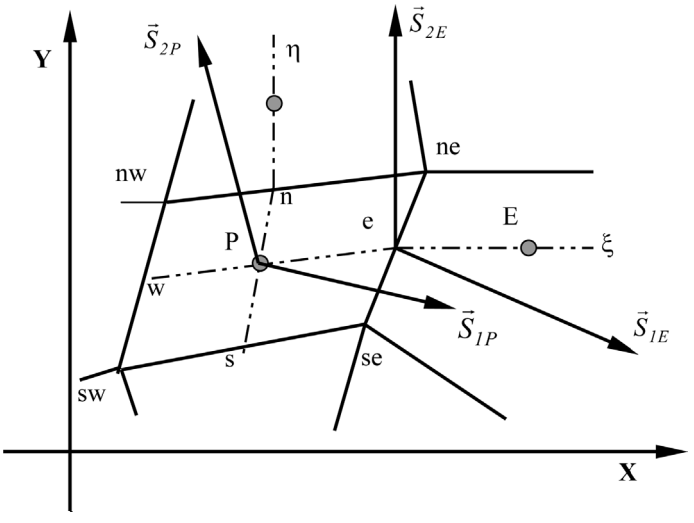

Figure 2.
A typical 2D-control volume and the notation for a Cartesian grid

where $\mathbf{S_{1e}}$ is the surface vector representing the area of the cell face (ξ = const) and S^x_{1e} and S^y_{1e} denotes its Cartesian components. These are given in terms of the CV vertex coordinates as follows:

$$S^x_{1e} = (y_n - y_s) \quad \text{and} \quad S^y_{1e} = -(x_n - x_s). \tag{11}$$

The mean cell face velocity components, U_e and V_e are obtained by interpolating neighbors' nodal values in a way, which ensures the stability of grid scheme. The convection flux of any variable ϕ can be expressed as:

$$F^C_e = \int_{S_e} \rho\phi V \, dS \approx (\rho\phi V)_e S_{1e} = \dot{m}_e \phi_e. \tag{12}$$

The diffusion flux of ϕ is calculated as:

$$F^D_e = -\int_{S_e} \Gamma_\phi \, \text{grad}\, \phi \, dS \approx -(\Gamma_\phi \, \text{grad}\, \phi)_e S_{1e}. \tag{13}$$

By expressing the gradient of ϕ at the cell face center "e", which is taken here to represent the mean value over the whole cell face, through the derivatives in ξ and η directions (Figure 2) and by discretizing these derivatives with CDS, the following expression results:

$$F^D_e \approx \frac{\Gamma_{\varphi.e}}{\mathbf{S_{1e}} \cdot \mathbf{PE}} [(\phi_E - \phi_P)(\mathbf{S_{1e}} \cdot \mathbf{S_{1e}}) + \underline{(\phi_n - \phi_s)_e (\mathbf{S_{1e}} \cdot \mathbf{S_{2e}})}]. \tag{14}$$

where **PE** is the vector representing the distance from P to E, directed towards E. $\mathbf{S_{2e}}$ is the surface vector orthogonal to **PE** and directed outwards positive η

coordinate (Figure 2), representing the area in the surface $\eta = 0$ bounded by P and E. Its x and y components are:

$$S_{2e}^{x} = -(y_E - y_P) \quad \text{and} \quad S_{2e}^{y} = (x_E - x_P). \tag{15}$$

The volumetric source term is integrated by simply multiplying the specific source at the control volume center P (which is assumed to represent the mean value over the whole cell) with the cell volume i.e.

$$Q_{\phi}^{q} = \int_V q_{\phi}\, \mathrm{d}V \approx (q_{\phi})_P \Delta V. \tag{16}$$

The pressure term in the momentum equations are treated as body force and may be regarded as pressure sources for the Cartesian velocity components. They are evaluated as:

$$\begin{aligned} Q_{u_i}^{p} &= -\int_S p\mathbf{i_i}\, \mathbf{dS} = -\int_V (\mathrm{grad}\, p\mathbf{i_i})\, \mathrm{d}V \\ &\approx -[(p_e - p_w)\mathbf{S_{1P}} + (p_n - p_s)\mathbf{S_{2p}}] \cdot \mathbf{i_i}. \end{aligned} \tag{17}$$

where the surface vectors $\mathbf{S_{1p}}$ and $\mathbf{S_{2p}}$ represent the area of the CV cross section at $\xi = 0$ and $\eta = 0$. respectively. Since CV's are bounded by straight lines, these two vectors can be expressed through the CV surface vectors, e.g. $\mathbf{S_{1P}} = (\mathbf{S_{1e}} + \mathbf{S_{1w}})/2$. Terms in the momentum equations, not featuring in equation (9), are discretized using the same approach and added to the source term. After summing up all cell face fluxes and sources, the discretized transport equation reduces to the following algebraic equation:

$$A_P \phi_P + \sum_{nb} A_{nb} \phi_{nb} = Q_{\phi}. \tag{18}$$

where the coefficients A_{nb}, contains the convective and diffusive flux contributions and Q_{ϕ} represents the source term. The system of equations is solved by using Stone's SIP solver.

Discretized momentum equations lead to an algebraic equation system for velocity components U and V where pressure, temperature, and fluid properties are taken from the previous iteration except the first iteration where initial conditions are applied. These linear equation systems are solved iteratively (inner iteration) to obtain an improved estimate of velocity. The improved velocity field is then used to estimate new mass fluxes, which satisfy the continuity equation. Pressure-correction equation is then solved using the same linear equation solver and to the same tolerance. Energy equation is then

solved in the same manner to obtain better estimate of new solution. Then the above procedure is repeated for a new time step. For time marching, we selected *Three Time Level Method* which is a fully implicit scheme of second order accurate. Iteration is continued until the difference between the two consecutive field values of variables is less than or equal to 10^{-5}.

Accuracy

In the present investigation, five combinations (20×10, 40×20, 80×40, 160×80, and 320×160) of control volumes are used to test the effect of grid size on the accuracy of the predicted results. Figure 3 shows the distribution of average Nusselt numbers of the hot wall as a function of grid sizes for four different Rayleigh numbers. It is clear from the figure that at lower Rayleigh number, average Nusselt number is almost independent of grid sizes. At higher Rayleigh numbers, the two higher grid sizes (160×80 and 320×160) give almost the same result. It is well known that the high mesh refinement always provides better result in the finite-volume method. The main disadvantage in taking higher mesh number is the increase in calculation time, which can be reduced by using a higher speed of Pentium processor. Our goal was to get better results. Thus, throughout this study, the results are presented for 320×160 CVs' for better accuracy. Predicted results of average Nusselt numbers for a square cavity ($A = 1.0$. $\lambda = 0$) with the same boundary conditions are compared with the results given by Bejan (1984) and Ozisik (1985). Comparisons are shown in Figure 4, where average Nusselt number is plotted as a function of Rayleigh number. Predicted results show a very good agreement with the result of Ozisic at lower Rayleigh number, but differ from Bejan's prediction. At higher Rayleigh number, present prediction shows better agreement with Bejan compared to Ozisic's results.

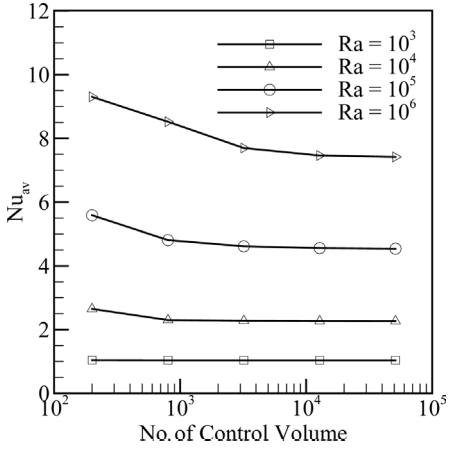

Figure 3.
Variation of average Nusselt number as a function of number of CV for $A = 0.25$ and $\lambda = 0.05$

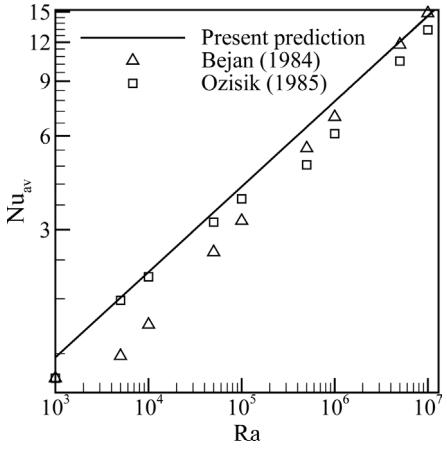

Figure 4.
Validation of average Nusselt number for $A = 0.25$ and $\lambda = 0.0$ with other reference work

Results and discussions

Flow and thermal field

The flow pattern inside the wavy enclosure and the temperature profile are presented in terms of streamlines and isothermal lines in Figure 5(a)-(d) for $A = 0.25$. $\lambda = 0.10$ at four selected Rayleigh numbers. At low Rayleigh number when convection current inside the cavity is comparatively weak, fluid stream near the hot wall tends to move towards the centerline or crest of the cavity were two streams from the opposite direction mix and rise upwards. Two counter-rotating vortices with small cores are observed on the flow field were bi-cellular flow pattern divides the cavity into two symmetric parts with respect to the centerline ($X^* = 0.5$) of the cavity. Due to the uniform temperature gradient at low Rayleigh number ($= 10^3$) circulation inside the cavity is very weak. Convection is less prominent at this Rayleigh number and heat transfer is mainly dominated by conduction. The basic difference between the isotherms in a wavy cavity with other geometry is their shape. Isothermal lines are nearly parallel to each other and follow the geometry of the wavy surfaces. A further increase of Rayleigh numbers increases the circulation strength inside the cavity. $Ra = 10^4$ is also characterized by the bi-cellular flow pattern, but thermal field is completely different compared to $Ra = 10^3$. Here, uniform temperature profile is changed and three high gradient spot is observed due to rapid circulation of fluid inside the cavity. Isotherms turn up (convective distortion) towards the cold wall due to the strong influence of the convection current. At $Ra = 10^5$. multi-cellular flow appears with four vortices. Due to comparatively high buoyant effect, another vertical stream of the fluid appears near the adiabatic walls. A periodic swirling of the isothermal lines appear at $Ra = 10^5$ due to the appearance of multi-cellular flow. Two high gradient spots appear near the bottom wall, where isothermal lines are concentrated. Heat transfer rate is higher in magnitude at that spots.

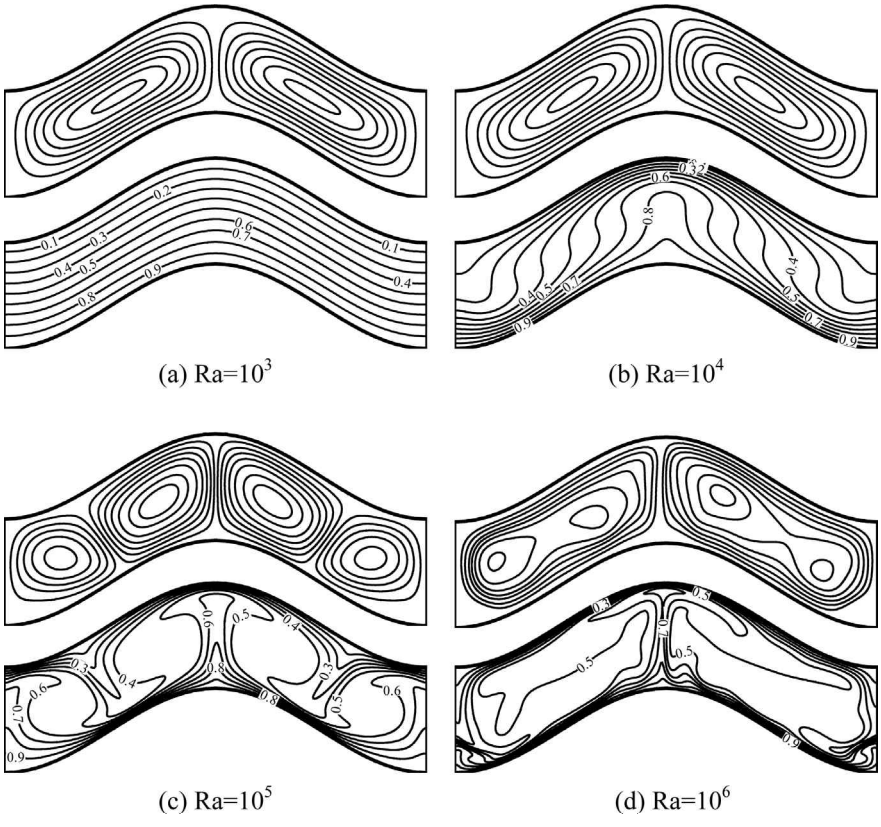

Figure 5.
Streamlines (top) and isothermal lines (bottom) for $A = 0.25$ and $\lambda = 0.10$

Further increase of Rayleigh number, increases the strength of the vortices, where four-cell multi-cellular flow pattern turns into two cell bi-cellular pattern. This bi-cellular flow pattern is qualitatively different from the flow pattern at low Rayleigh number. Periodic swirling nature of isothermal lines disappears due to the occurrence of reverse transition in flow field. Hot spots almost occupy the bottom wall of the cavity.

Transition of cell mode

The problem of the onset of hydrodynamic and thermal instabilities in the horizontal layers of fluid heated from bellow is well suited to illustrate the many facets, mathematical and physical, of the general theory of hydrodynamic stability. Specially, many aspects of the stability (or instability) of the fluid-layer trapped between the two rigid walls (bottom hot and top cold) have been treated by many researchers over the last 100 years (for example, see Chandrasekhar, 1961). The transition of cell mode of the fluid inside two rigid walls (in Rayleigh-Benard convection) is also a well established problem. However, a mathematical analysis to predict the transition parameter

(for example, the critical Rayleigh number) and the physical mechanism is an extremely challenging task in the case of wavy walled enclosure under the Rayleigh-Benard convection like situation due to the presence of two additional parameters (A and λ). Instead of performing a linear stability analysis, we modified our numerical algorithm for post processing (a programme written in FORTRAN77 and connected to the software Tecplot 8) to predict the transition between unicellular flow to bicellular or multicellular flow. Initially, for constant λ and A, the flow solver is executed for a range of Rayleigh numbers keeping a considerably large gap between the two consecutive Rayleigh numbers (50-100 depending on the value λ). Once we get a rough picture of the transition of cell mode, we re-execute the flow solver for a small range of Rayleigh numbers keeping a comparatively small gap between the two consecutive Rayleigh numbers (1–5). For example, when $\lambda = 0.01$ and $A = 0.25$. the magnitude of the starting Rayleigh number for the flow solver is 1,700. Note that the first critical Rayleigh number for the Rayleigh-Benard convection with rigid walls is 1,708 (Chandrasekhar, 1961). Figure 6(a)-(h) shows the cell pattern for $\lambda = 0.01$ and $A = 0.25$ for eight selected values of Rayleigh number. A symmetric bicellular flow pattern characterizes the flow filled inside the cavity until the value of Rayleigh number reaches 1,905. Two additional cells appear near the adiabatic walls (Figure 6(d)) at which the

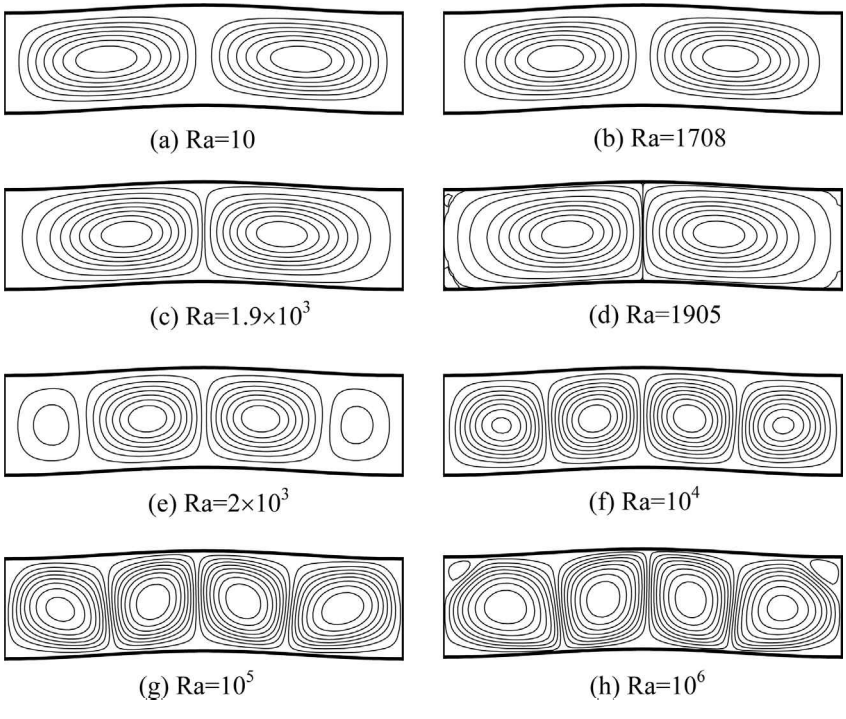

Figure 6.
Variation of cell pattern inside a cavity with $\lambda = 0.01$ and $A = 0.25$ for different Rayleigh number

Rayleigh number changes the bicellular flow into a four-cell multicellular flow. These cells grow in size with the increasing Rayleigh number, but growth rate of the cells becomes slower when Ra approaches 10^4. A second transition of the cell mode is observed near Ra = 10^6. The overall cell modes and their transitions are shown in Figure 7. Note that a non-uniform scale is selected for Rayleigh numbers in the abscissa of the Figure 7 for convenience. However, this scenario is completely different for $\lambda = 0.125$ as shown in Figures 8 and 9. The symmetric bicellular flow changes into an asymmetric tricellular flow around Ra = 13.995. This tricellular flow pattern remains unchanged for a small interval of Rayleigh number (Ra = 13.995 – 14.877). Then a second transition makes it to a four-cell multicellular flow pattern. A reverse transition occurs around Ra = 10^6. The overall cell modes and their transitions are shown in Figure 9 for this case.

Heat transfer

Heat transfer is calculated in terms of local (Nu_L) and average (Nu_{av}) Nusselt numbers using the following equations

$$Nu_L = \frac{\delta}{k} h_L = \frac{\delta}{k}\left\{\frac{k}{\Delta T}\left(\frac{dT}{dn}\right)_w\right\} = \left(\frac{d\Theta}{d\hat{n}}\right)_w. \tag{19}$$

$$Nu_{av} = \frac{1}{S}\int_0^S Nu_L \, ds \tag{20a}$$

$$S = \int_0^1 \sqrt{1 + \left(\frac{dY^*}{dX^*}\right)^2}\, dX^* = \frac{\text{EllipticE}\left(2\pi\sqrt{-\lambda^2}\right)}{\pi}. \tag{20b}$$

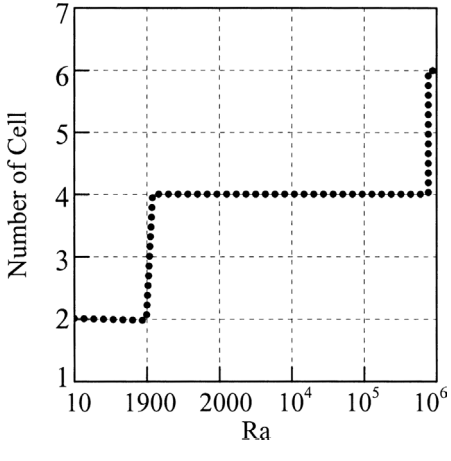

Figure 7.
Transition of the cell mode as a function of Rayleigh number for $\lambda = 0.01$ and $A = 0.25$

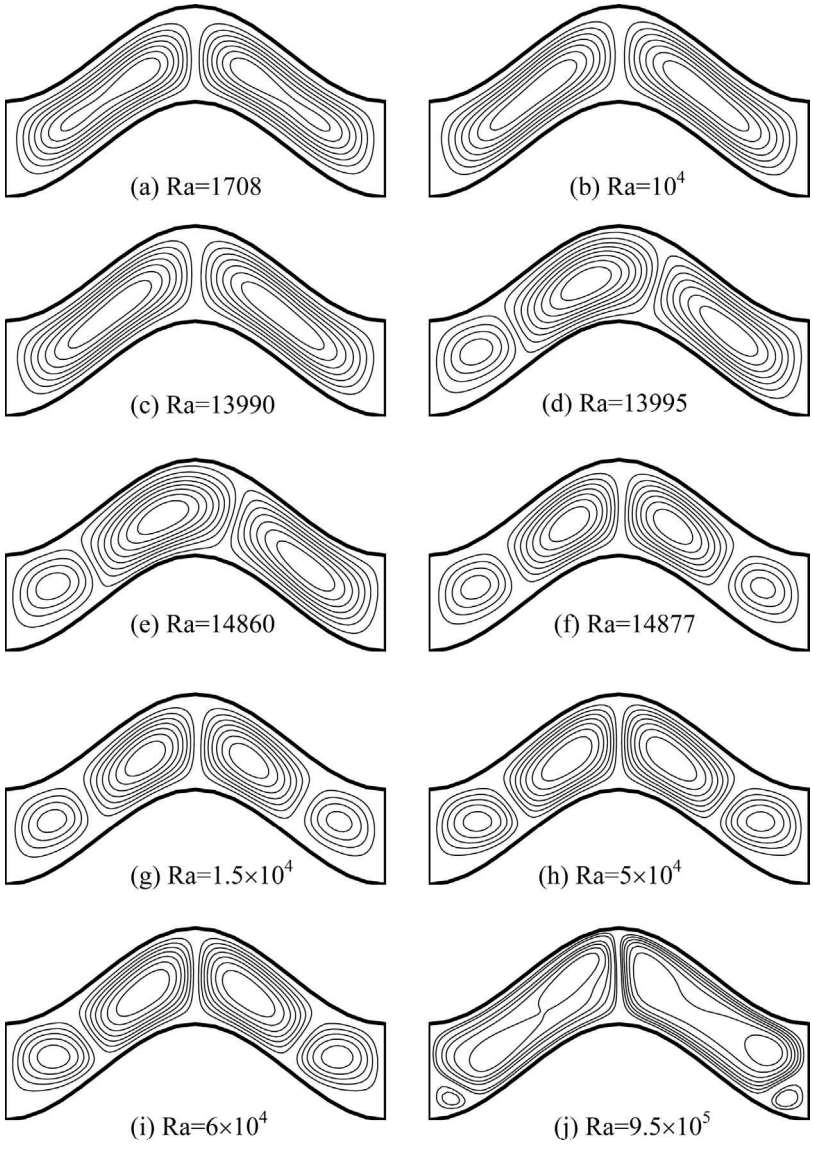

Figure 8.
Variation of cell pattern inside a cavity with $\lambda = 0.125$ and $A = 0.25$ for different Rayleigh number

where the special function "**EllipticE**" is the elliptic integral of second kind (Abramowitz and Stegun, 1965). Local Nusselt number distribution is presented in Figures 10 and 11. Average Nusselt number distribution is presented in Figures 12-14. Detail discussions on heat transfer is presented in the following two paragraphs.

Local Nusselt number distribution along the hot wavy wall is shown in Figure 10 for a constant Rayleigh number and four selected surface waviness

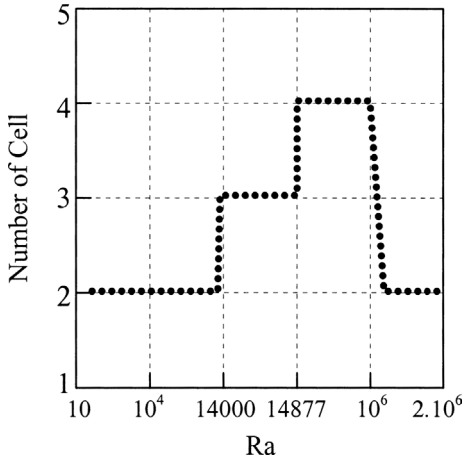

Figure 9.
Transition of the cell mode as a function of Rayleigh number for $\lambda = 0.125$ and $A = 0.25$

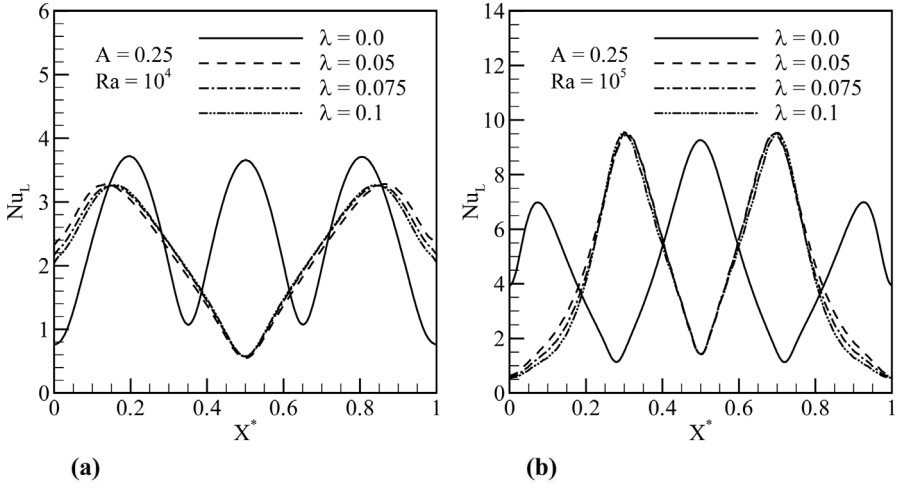

Figure 10.
Change of the local Nusselt number along the length of the bottom wave

Note: The variations of the local Nusselt number with scaled wavelength inside the wavy enclosure are depicted for a fixed aspect ratio (A) of 0.25 and a fixed Rayleigh number (a) $Ra = 10^4$, (b) $Ra = 10^5$. Different line types correspond to different surface waviness of the enclosure as indicated in the legend

($\lambda = 0.0$. 0.05, 0.075, 0.1) for an aspect ratio, $A = 0.25$. At $Ra = 10^4$. heat transfer rate shows true periodic nature with respect to the axial distance along the length of the bottom wall for $\lambda = 0.0$. where three peaks represent not only the three spots of highest temperature gradient, but also characterize three pairs of cell generated due to the fluid motion inside the cavity. However, for $\lambda = 0.05$. 0.075, 0.1 local Nusselt number distribution changed significantly due to low temperature gradient at the midpoint of the cavity. In that case, heat

transfer rate increases up to the $X^* = 0.15$ and falls along the wavy wall gradually up to the midpoint ($X^* = 0.5$) of the cavity. This nature is similar for other surface waviness with a slight variation in magnitudes. Completely different picture is observed at $Ra = 10^5$. For $\lambda = 0.0$. three peaks again represent the three spots of highest temperature gradient with a higher temperature gradient at the mid point of the wave.

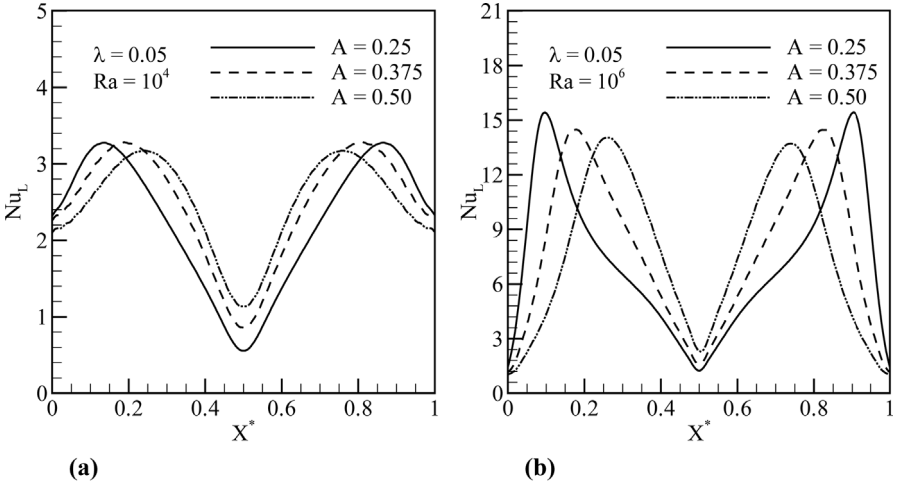

Figure 11.
Change of the local Nusselt number along the length of the bottom wave

Note: The variations of the local Nusselt number with scaled wavelength inside the wavy enclosure are depicted for a fixed surface waviness (λ) of 0.05 and a fixed Rayleigh number (a) $Ra = 10^4$, (b) $Ra = 10^5$. Different line types correspond to different aspect ratio of the enclosure as indicated in the legend

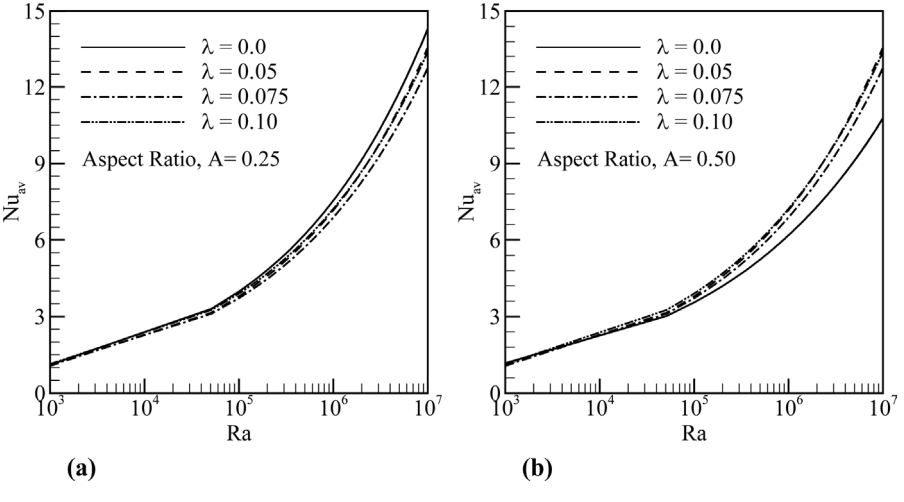

Figure 12.
Nusselt number as a function of Rayleigh number for different surface waviness for two fixed aspect ratio: (a) $A = 0.25$. and (b) $A = 0.50$

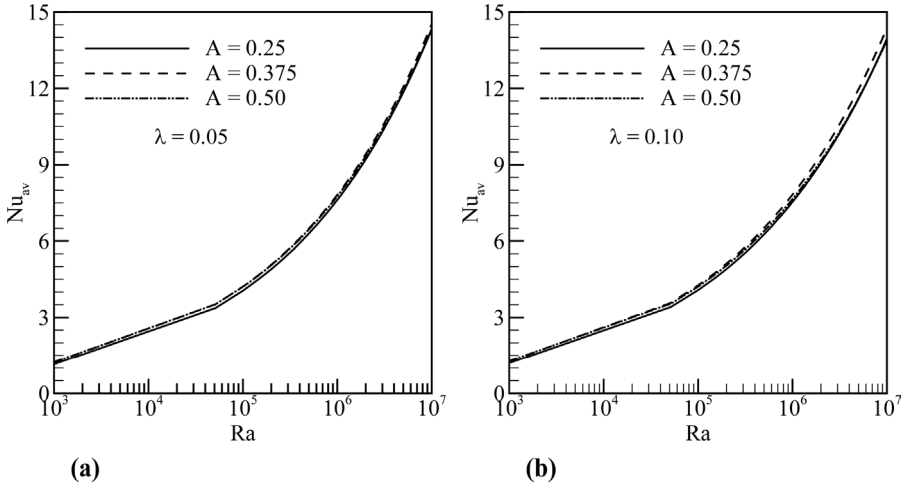

Figure 13.
Nusselt number as a function of Rayleigh number for different aspect ratio for two fixed surface waviness: (a) $\lambda = 0.05$. and (b) $\lambda = 0.10$

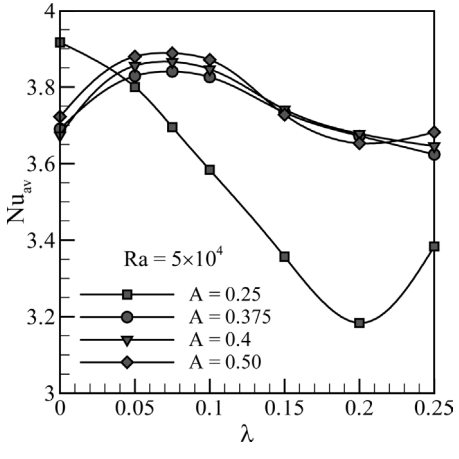

Figure 14.
Nusselt number as a function of surface waviness for fixed Rayleigh number ($Ra = 5 \times 10^4$). Two lines correspond to two different aspect ratio of the enclosure as indicated in the legend

Figure 11 depicts the extent to which the local Nusselt number distribution is affected by changes in the aspect ratio. We observed that at $Ra = 10^4$. two peaks move towards the center of the cavity with the increase of aspect ratio. Similar pattern was observed at $Ra = 10^6$. but the magnitude of the two peak is higher. It is also noticed that heat transfer rate is faster near the straight wall and decrease rapidly with the increase of X^*. Whatever be the values of aspect ratio, heat transfer rate is always minimum at the mid point of the bottom wall.

Local Nusselt numbers are integrated to calculate the average value of the Nusselt number according to equation (20). Average Nusselt number is plotted as a function of Rayleigh number in Figure 12 for two fixed aspect ratios, $A = 0.25$ and 0.50, for different surface waviness. At lower Rayleigh number,

the change of average heat transfer is almost negligible. However, at higher Rayleigh number this effect is quite significant. At higher surface waviness ratio heat transfer rate is higher at higher Rayleigh number when surface waviness ratio increase from zero to other values and then, further increases of surface waviness ratio which shows a negligible effect on average heat transfer rate. But for $A = 0.5$. different scenario is observed at higher Rayleigh number though the similar trend is observed at lower higher Rayleigh number. Here, heat transfer rate increases with the increase of surface waviness ratio which increase from zero to other values.

Effect of aspect ratio

Figure 13 depicts the variation of average Nusselt number as a function of the Rayleigh number for three different aspect ratios, $A = 0.25$. 0.375, and 0.5 and a constant surface waviness. Two sets of results are shown, those corresponding to $\lambda = 0.05$ in Figure 13(a), and $\lambda = 0.10$ in Figure 13(b). From Figure 13(a) it is clear that the change of heat transfer rate is negligible with changes of aspect ratio of a wavy enclosure. A tiny increase of heat transfer rate is obtained at higher aspect ratio. For $\lambda = 0.10$. similar trend is observed with slightly better variation of heat transfer with aspect ratio. Magnitudes of average Nusselt number are slightly higher for higher aspect ratio at higher Rayleigh number.

Effect of surface waviness

Figure 14 shows the variation of average Nusselt number for a hot wall as a function of surface waviness (λ) for $Ra = 5 \times 10^4$. Four lines correspond to four different aspect ratios of the enclosure as indicated in the legend where symbols show the data points and lines are the best fitted curve. We observe completely a different picture for different aspect ratios at lower surface waviness ratio. At $A = 0.25$. heat transfer rate decrease rapidly with the increase of surface waviness, but after a certain waviness ($\lambda \geq 0.2$). heat transfer rate increases. At $\lambda = 0.2$. we observed the minimum heat transfer compared to other values of surface waviness. Completely different nature is observed on the heat transfer rate for $A = 0.5$. When surface waviness increases from zero to another value, heat transfer also increases following which the negligible variation is obtained for $0.05 < \lambda < 0.1$. Further increase of surface waviness causes the decrease of heat transfer rate up to $\lambda \approx 0.2$. after which the heat transfer rate again goes up.

Axial velocity profiles

For three selected Rayleigh numbers ($= 10^4$, 10^5, and 10^6), axial velocity profiles are shown in Figure 15(a)-(c) at six locations along the axial direction (X^*) and for a constant surface waviness ($\lambda = 0.1$). Velocity profiles are symmetric in the vertical centerline ($X^* = 0.5$) of the cavity for all the values of the Rayleigh number. We only concentrate about our discussions on the left portion of the

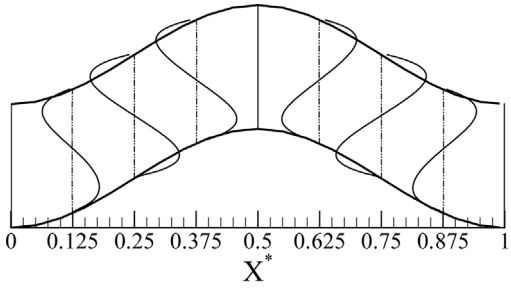

(a) Ra=10^4, λ=0.1

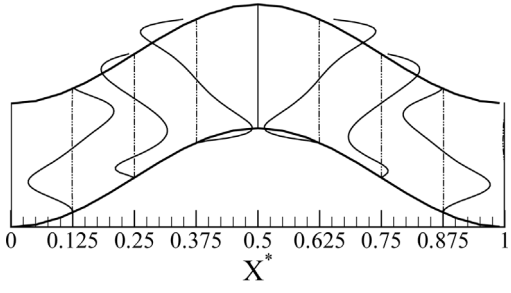

(b) Ra=10^5, λ=0.1

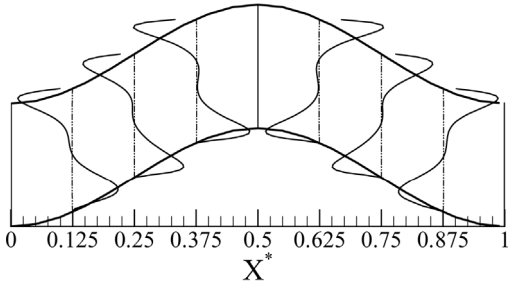

(c) Ra=10^6, λ=0.1

Figure 15.
Axial velocity profiles at X^* = 0.125. 0.25, 0.375, 0.50, 0.625, 0.75 and 0.875 for Ra = 10^4. 10^5, and 10^6 and λ = 0.10

cavity about the vertical centerline. Vertical line (dash-dot-dot) with each profiles indicate a reference line where axial velocity is zero. At Ra = 10^4 (Figure 15(a)), an S-shaped velocity profile resembles to the sinusoidal distribution of the velocity along the vertical direction which is a characteristic distribution of the velocity for shallow cavities. Velocity profiles support the bi-cellular flow pattern (see streamlines in Figure 5(b)) inside the cavity at this Rayleigh number. Magnitude of the velocity decreases towards the adiabatic walls and the vertical centerline of the cavity. Appearance of multi-cellular flow (see streamlines in Figure 5(c)) dramatically changes the pattern of axial

velocity profile as shown in Figure 15(b). Considering the left half of the cavity, the vortex near the adiabatic wall is rotating clockwise and near the vertical symmetry line it is in the counterclockwise direction. Locations $X^* = 0.125$ and 0.375 coincide with the clockwise and counterclockwise vortices, respectively. This is the main reason for the opposite nature of profiles at these two locations. However, most of the upper parts of the location $X^* = 0.25$ (see also Figure 5(c)) are occupied by the counterclockwise vortex. Only a small part near the bottom wall is shared by the clockwise vortex. This common sharing by two vortices occurs due to the presence of the wavy nature of the top and the bottom walls, which is absent (no sharing) in the case of the cavity with flat walls. Axial velocities at the upper part of the location $X^* = 0.25$ form the usual S-shaped profile. A small portion near the bottom wall shows negative velocities due to the interference of the clockwise vortex. Flow at $\mathrm{Ra} = 10^6$ is bi-cellular (see Figure 5(d)) and this is qualitatively different from the flow feature at $\mathrm{Ra} = 10^4$ (which is also bi-cellular in nature). This is the boundary layer regime of the flow and velocity profiles which are characterized by high near-wall-gradient along with almost zero velocity at the center of the cavity.

Heat transfer irreversibility

Any heat transfer problem is always accompanied by entropy generation, hence by the one-way destruction of available work (Bejan, 1996). Entropy generation is related to the thermodynamic imperfection of a real device and, in the long run, is a real cause for the inherent irreversibility of such devices. Therefore, it makes good engineering sense to focus on the irreversibility of heat transfer processes and try to understand the function of the entropy generation mechanism. The starting point of the irreversibility analysis is a perfect description of the local entropy generation rate and according to Bejan (1996), the local rate of entropy generation can be written as

$$\dot{S}'''_{\mathrm{gen}} = \frac{k}{T_0^2}\left[\left(\frac{\partial T}{\partial x}\right)^2 + \left(\frac{\partial T}{\partial y}\right)^2\right] + \frac{\mu}{T_0}\left[2\left\{\left(\frac{\partial u}{\partial x}\right)^2 + \left(\frac{\partial v}{\partial y}\right)^2\right\} + \left(\frac{\partial u}{\partial y} + \frac{\partial v}{\partial x}\right)^2\right] \tag{21}$$

where T_0 is the reference temperature. Using the same *characteristic parameters* already used for the dimensionless purpose, the non-dimensional form of equation (21) is

$$N_{\mathrm{S}} = \left[\left(\frac{\partial \Theta}{\partial X}\right)^2 + \left(\frac{\partial \Theta}{\partial Y}\right)^2\right] + \frac{\mathrm{Br}}{\Omega}\left[2\left\{\left(\frac{\partial U}{\partial X}\right)^2 + \left(\frac{\partial V}{\partial Y}\right)^2\right\} + \left(\frac{\partial U}{\partial Y} + \frac{\partial V}{\partial Y}\right)^2\right] \tag{22}$$

where N_{S}, *Br*, and Ω represent entropy generation number, the Brinkman number, and dimensionless temperature difference, respectively. Entropy

generation number (N_S) is a ratio between the local entropy generation rate ($\dot{S}'''_{gen}$) and a characteristic entropy transfer rate ($\dot{S}'''_0$) which is shown in the following equation

$$N_S = \frac{\dot{S}'''_{gen}}{\dot{S}'''_0}; \quad \text{where} \quad \dot{S}'''_0 = \frac{k(\Delta T)^2}{\delta^2 T_0^2} \tag{23}$$

The dimensionless form of the entropy generation rate (N_S), given in equation (22), consists of two parts. The first part (first square bracketed term at the right-hand side of equation (22)) is the irreversibility due to finite temperature gradient and generally termed as heat transfer irreversibility (HTI). The second part is the contribution of fluid friction irreversibility (FFI) to entropy generation, which can be calculated from the second square bracketed term. The overall entropy generation, for a particular problem, is an internal competition between HTI and FFI. Usually, free convection problems, at low and moderate Rayleigh numbers, are dominated by the HTI (discussed later in detail). Entropy generation number (N_S) is good for generating entropy generation profiles or maps, but fails to give any idea whether fluid friction or heat transfer dominates. Bejan (1979) proposed irreversibility distribution ratio (Φ), which is the ratio between FFI and HTI. As an alternative irreversibility distribution parameter, Paoletti *et al.* (1989) defined Bejan number (Be), which is the ratio of HTI to the total entropy generation. Mathematically, Bejan number becomes

$$\text{Be} = \frac{\text{HTI}}{\text{HTI} + \text{FFI}} = \frac{1}{1 + \Phi} \tag{24}$$

Bejan number ranges from 0 to 1. Accordingly, Be = 1 is the limit at which the HTI dominates, Be = 0 is the opposite limit at which the irreversibility is dominated by fluid friction effects, and Be = 1/2 is the case in which the heat transfer and fluid friction entropy generation rates are equal.

For a fixed aspect ratio ($A = 0.25$). contours of Bejan numbers are presented in Figure 16(a)-(f) for Ra = 10^4 and 10^5 and λ = 0.0. 0.05, and 0.1. Whatever the values of Ra, λ, and A, be regions near the top and the bottom walls always act as strong concentrators of HTI. The maximum value of Bejan contour (Be_{max}) appears in the immediate neighborhood of the top and the bottom walls. At Ra = 10^4 and λ = 0.0 (Figure 16(a)), HTI is characterized by three spots of "Highly-Concentrated-Bejan-Contours (HCBC)" near the top wall and two spots near the bottom wall. To understand HTI, as shown by Bejan contour in Figure 16(a), in detail first focus on Figure 17 (we will go through Figure 16(a)-(f) next). To ease our understanding about Figure 16(a), we introduce field of streamlines and isothermal lines along with the constant Bejan number contours in Figure 17. We will first focus our attention on the three spots marked by ellipse (E1, E2 and E3). This is a case of multicellular

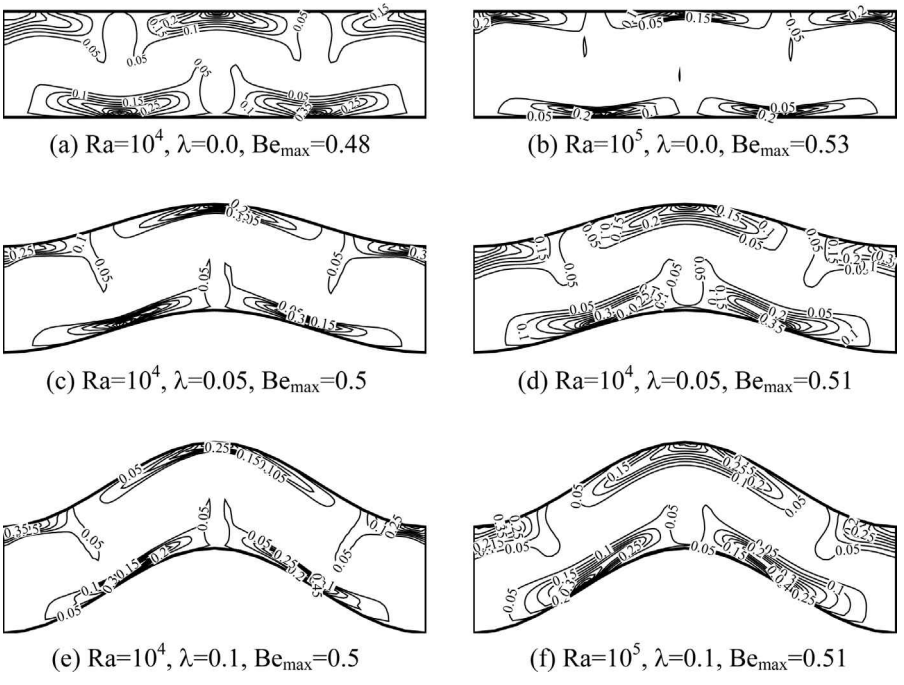

Figure 16.
Contours of Bejan number for $A = 0.25$

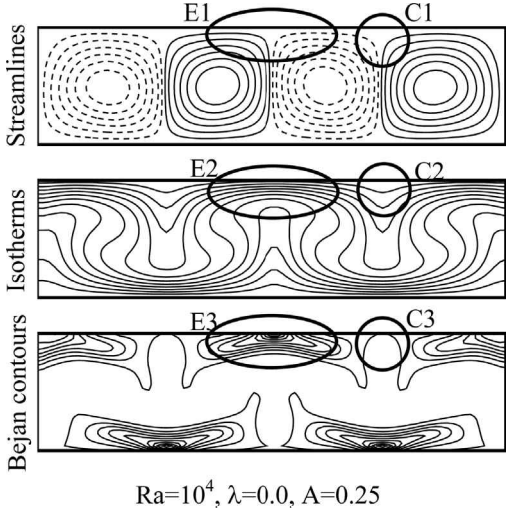

Figure 17.
A combined plot of streamlines, isothermal lines, and constant Bejan number contour for Ra = 10^4. $\lambda = 0.0$. and $A = 0.25$

flow with four vortices. Dashed lines indicate the clockwise rotation and solid lines indicate the counterclockwise rotation. Fluid region marked by E1 is forced upward direction. At this Rayleigh number (= 10^4) convection current is well set and strong enough to cause the swirl (convective distortion) in isothermal lines. Isothermal lines are heavily concentrated inside the region spotted by E2. This is the region with high temperature gradient, which causes high HTI (E3). Next focus on the spots marked by circle (C1, C2, and C3). Obviously, two downward streams of fluid (C1) cause very low temperature gradient near the top wall (C2) and which leaves a region of low HTI (C3). A spatially periodic region, extended along the horizontal centerline of the cavity, shows very low irreversibility (HTI) due the lower temperature gradients. Such region is defined as an *idle region for irreversibility* (Mahmud and Fraser, 2002a, b). A thin extension of the idle region for irreversibility exists between the two consecutive spots of HCBC at the top and the bottom walls.

At Ra = 10^5 (Figure 16(b)), spots of HCBC elongates along the horizontal direction and at the same time concentrates more towards the walls. Now, three spots of HCBC exist near the top wall and two near the bottom wall. Idle region for irreversibility occupies more area inside the enclosure. An introduction of the surface undulant dramatically changes the characteristic features of the HTI inside the enclosure. Three spots of HCBC at the top wavy wall and two at the bottom wavy wall are observed at Ra = 10^4 for $\lambda = 0.05$ (Figure 16(c)). Focusing first on the top wavy wall, the extension of HTI is higher near the middle part of the wall than the part near the adiabatic walls. However, at the bottom wavy wall zones of high HTI are symmetric (and also equal in size) with respect to the vertical centerline of the cavity. For $\lambda = 0.1$ (Figure 16(e)), spots of HCBC occupy slightly more region near the top and bottom wavy walls when compared with the case $\lambda = 0.05$. For Ra = 10^5 (Figure 16(d) and (f)), HTI scenarios remain the same as in the case of Ra = 10^4. but now spots of HCBC concentrate more towards the wavy walls.

Conclusion

Laminar steady natural convection heat transfer and fluid flow inside a wavy enclosure with two wavy walls and two straight walls are investigated numerically. The effect of aspect ratio and surface waviness on heat transfer and HTI is tested at different Rayleigh numbers. Aspect ratio does not play any important role on the heat transfer inside a wavy enclosure of fixed surface waviness, but when surface waviness changes from zero to a certain value, aspect ratio dominates the heat transfer characteristics. The lower the surface waviness, the higher is the heat transfer for lower aspect ratio, but this statement flipped for higher aspect ratio. At higher aspect ratio, heat transfer increases with the increase of surface waviness. For a constant Rayleigh number, heat transfer falls gradually with an increasing surface waviness up to

a certain value of surface waviness, above which heat transfer increases again for low aspect ratio. Whereas for higher aspect ratio, heat transfer gradually increases with an increase of surface waviness up to a certain value of surface waviness and subsequently heat transfer falls gradually upto certain waviness, above which heat transfer increases again like the other case.

References

Abramowitz, M. and Stegun, I. (1965), "Elliptic Integrals", *Handbook of Mathematical Functions*, Chapter 17, Dover Publications, New York.

Adjlout, L., Imine, O., Azzi, A. and Belkadi, M. (2002), "Laminar natural convection in an inclined cavity with a wavy wall", *Int. J. Heat Mass Transfer*, Vol. 45, pp. 2141-52.

Asako, Y. and Faghri, M. (1987), "Finite volume solution for laminar flow and heat transfer in a corrugated duct", *J. Heat Transfer*, Vol. 109, pp. 627-34.

Aydin, O., Unal, A. and Ayhan, T. (1999), "A numerical study on buoyancy-driven flow in an inclined square enclosure heated and cooled on adjacent walls", *Numerical Heat Transfer (Part A)*, Vol. 36, pp. 585-899.

Bejan, A. (1979), "A study of entropy generation in fundamental convective heat transfer", *J. Heat Transfer*, Vol. 101, pp. 718-25.

Bejan, A. (1984), *Convective Heat Transfer*, Wiley, New York.

Bejan, A. (1996), *Entropy Generation Minimization*, CRC Press, New York.

Chandrasekhar, S. (1961), *Hydrodynamic and Hydromagnetic Stability*, Oxford University Press, London.

Chen, C.L. and Cheng, C.H. (2002), "Buoyancy-induced flow and convective heat transfer in an inclined arc-shape enclosure", *Int. J. Heat Fluid Flow*, Vol. 23, pp. 823-30.

Das, P.K. and Mahmud, S. (2003), "Numerical investigation of natural convection inside a wavy enclosure", *Int. J. Thermal Sciences*, Vol. 42, pp. 397-406.

Elsherbiny, S.M. (1996), "Free convection in inclined air layers heated from above", *Int. J. Heat Mass Transfer*, Vol. 39, pp. 3925-30.

Ferziger, J. and Peric, M. (1996), *Computational Methods for Fluid Dynamics*, Springer Verlag, Berlin.

Hadjadj, A. and Kyal, M.E. (1999), "Effect of two sinusoidal protuberances on natural convection in a vertical annulus", *Numerical Heat Transfer (Part A)*, Vol. 36, pp. 273-89.

Hamady, F.J., Lloyd, J.R., Yang, H.Q. and Yang, K.T. (1989), "Study of local natural convection heat transfer in an inclined enclosure", *Int. J. Heat Mass Transfer*, Vol. 32, pp. 1697-708.

Hortmann, M., Peric, M. and Scheuerer, G. (1990), "Finite volume multigrid prediction of laminar natural convection: Benchmark solutions", *Int. J. Numer. Methods Fluids*, Vol. 11, pp. 189-207.

Hossain, M.A. and Rees, D.A.S. (1999), "Combined heat and mass transfer in natural convection flow from a vertical wavy surface", *Acta Mechanca*, Vol. 136, pp. 133-41.

Kumar, B.V.R. (2000), "A study of free convection induced by a vertical wavy surface with heat flux in a porous enclosure", *Numerical Heat Transfer (Part A)*, Vol. 37, pp. 493-510.

Lage, J.L. and Bejan, A. (1990), "Convection from a periodically stretching plane wall", *J. Heat Transfer*, Vol. 112, pp. 92-9.

Leneweit, G. and Auerbach, D. (1999), "Detachment phenomena in low Reynolds number flows through sinusoidally constricted tube", *J. Fluid Mechanics*, Vol. 387, pp. 129-50.

Mahmud, S. (2002), "Free convection inside an L-shaped enclosure", *Int. Comm. Heat Mass Transfer*, Vol. 29, pp. 1005-13.

Mahmud, S. and Fraser, R.A. (2002a), "Second law analysis of heat transfer and fluid flow inside a cylindrical annular space", *Exergy: An International Journal*, Vol. 2, pp. 322-9.

Mahmud, S. and Fraser, R.A. (2002b), "Analysis of mixed convection-radiation interaction in a vertical channel: entropy generation", *Exergy: An International Journal*, Vol. 2, pp. 330-9.

Mahmud, S., Das, P.K., Hyder, N. and Islam, A.K.M.S. (2002c), "Free convection in an enclosure with vertical wavy walls", *Int. J. Thermal Sciences*, Vol. 41, pp. 440-6.

Mahmud, S., Islam, A.K.M.S. and Das, P.K. (2001), "Numerical prediction of fluid flow and heat transfer in a wavy pipe", *Int. J. Thermal and Fluid Sciences*, Vol. 10, pp. 133-8.

Mahmud, S., Islam, A.K.M.S. and Mamun, M.A.H. (2002a), "Separation characteristics of fluid flow inside two parallel plates with wavy surface", *Int. J. Engineering Science*, Vol. 40, pp. 1495-509.

Mahmud, S., Islam, A.K.M.S. and Mamun, M.A.H. (2002b), "Separation characteristics of fluid flow in a pipe with wavy surface", *Int. J. Appl. Mechanics and Engineering*, Vol. 7, pp. 1255-70.

Moulic, S.G. and Yao, L.S. (1989), "Natural convection along a wavy surface with uniform heat flux", *J. Heat Transfer*, Vol. 111, pp. 1106-8.

Ozisik, M.N. (1985), *Heat Transfer a Basic Approach*, McGraw-Hill, New York.

Ozoe, H., Sayma, H. and Churchill, S.W. (1975), "Natural convection in an inclined rectangular channel at various aspect ratios and angles – experimental measurements", *Int. J. Heat Mass Transfer*, Vol. 18, pp. 1425-31.

Paoletti, S., Rispoli, F. and Sciubba, E. (1989), "Calculation of exergetic losses in compact heat exchanger passages", *ASME AES.*, Vol. 10, pp. 21-9.

Peric, M. (1993), "Natural convection in trapezoidal cavities", *Numerical Heat Transfer (Part A)*, Vol. 24, pp. 213-9.

Poulikakos, D. and Bejan, A. (1983), "Natural convection in a triangular enclosure", *J. Heat Transfer*, Vol. 105, pp. 652-5.

Rees, D.A.S. and Pop, I. (1995), "Free convection induced by a vertical wavy surface with uniform heat transfer flux in a porous medium", *J. Heat Transfer*, Vol. 117, pp. 545-50.

Russ, G. and Beer, H. (1997a), "Heat transfer and flow field in a pipe with sinusoidal wavy surface-I. Numerical investigation", *Int. J. Heat Mass Transfer*, Vol. 40, pp. 1061-70.

Russ, G. and Beer, H. (1997b), "Heat transfer and flow field in a pipe with sinusoidal wavy surface-II. Experimental investigation", *Int. J. Heat Mass Transfer*, Vol. 40, pp. 1071-81.

Saidi, C., Legay, F. and Pruent, B. (1987), "Laminar flow past a sinusoidal cavity", *Int. J. Heat Mass Transfer*, Vol. 30, pp. 649-60.

Sobey, I.J. (1980a), "On flow through furrowed channels. Part 1. Calculated flow patterns", *J. Fluid Mechanics*, Vol. 96, pp. 1-26.

Sobey, I.J. (1980b), "On flow through furrowed channels. Part 2. Observed flow patterns", *J. Fluid Mechanics*, Vol. 96, pp. 27-32.

Sobey, I.J. (1982), "Oscillatory flows at intermediate Strouhal number in asymmetric channels", *J. Fluid Mechanics*, Vol. 125, pp. 359-73.

Sobey, I.J. (1983), "The occurrence of separation in oscillatory flow", *J. Fluid Mechanics*, Vol. 134, pp. 247-57.

Sundstrom, L.G. and Kimura, S. (1996), "On laminar free convection in inclined rectangular enclosures", *J. Fluid Mechanics*, Vol. 313, pp. 343-66.

Wang, G. and Vanka, S.P. (1995), "Convective heat transfer in periodic wavy passages", *Int. J. Heat Mass Transfer*, Vol. 38, pp. 3219-30.

Yang, K.T. (1987), "Natural convection in enclosures", in Kakac, S., Shah, R.K. and Aung, W. (Eds), *Handbook of Single-Phase Convective Heat Transfer*, Chapter 13, Wiley, New York.

Yao, L.S. (1983), "Natural convection along a vertical wavy surface", *J. Heat Transfer*, Vol. 105, pp. 465-8.